Solid-liquid Flow in Stirred Tanks: "CFD-grade" Experimental Investigation

Sommer, A.-E.; Rox, H.; Eckert, K.; Shi, P.; Rzehak, R.;

Originally published:

May 2021

Chemical Engineering Science 245(2021), 116743

DOI: https://doi.org/10.1016/j.ces.2021.116743

Perma-Link to Publication Repository of HZDR:

https://www.hzdr.de/publications/Publ-31701

Solid-liquid Flow in Stirred Tanks: "CFD-grade" Experimental Investigation

A.-E. Sommer[a,*], H. Rox[a], K. Eckert[a,b], P. Shi[a,c], R. Rzehak[a]

[a] *Helmholtz-Zentrum Dresden-Rossendorf, Institute of Fluid Dynamics, Bautzner Landstrasse 400, 01328 Dresden, Germany*
[b] *Technische Universität Dresden, Institute of Process Engineering and Environmental Technology, 01062 Dresden, Germany*
[c] *Technische Universität Dresden, Faculty of Mechanical Engineering, Institute of Power Engineering, 01062 Dresden, Germany*

Abstract

Computational Fluid Dynamics (CFD) simulations of the solid-liquid flow in stirred tanks are feasible with appropriate closure models. However, no systematic assessment of different models have appeared because of lacking validation data. The present study accumulates a "CFD-grade" database on single-phase and two-phase flows experiments in a stirred tank (diameter = 90 mm). The velocity fields of the liquid and the solid phase are measured with Particle Image Velocimetry and Particle Shadow Velocimetry, respectively. The experiments cover a range of parameters as density ratio ($\rho_S/\rho_L = 1.1 \ldots 2.5$), particle diameter ($63\,\mu\text{m} \ldots 500\,\mu\text{m}$), solid volume fraction ($0.025\,\text{vol}\% \ldots 0.1\,\text{vol}\%$) and impeller rotation speed ($650\,\text{rpm} \ldots 1500\,\text{rpm}$). The mean and fluctuating liquid and solid velocities are obtained as time-averaging and angle-resolved averaging, as well as the local solid fraction. The experimental data of the single phase flow is compared with CFD simulations and show a good predictions. A systematic assessment of CFD models for solid-liquid flows will appear as a sequel.

Keywords: stirred tanks, solid-liquid flow, Particle Image Velocimetry (PIV), Particle Shadow Velocimetry (PSV), "Computational Fluid Dynamics (CFD)-grade" database

1. Introduction

Stirred tanks are commonly used to suspend solid particles in a liquid in many branches of industry such as chemical engineering (Sardeshpande and Ranade, 2012), biotechnology (Trad et al., 2015) and minerals processing (Wu et al., 2011). Typical applications are heterogeneously catalyzed reactions, the production of bio-hydrogen, and separation by flotation. The turbulent flow induced by a mechanically rotating impeller enhances the solid-liquid heat and mass transfer. The quality of the suspension is the result of an intricate interplay between the two phases and depends on their turbulent characteristics. Consequently, turbulent solid-liquid stirred tanks have been widely studied using experimental approaches (Nouri and Whitelaw, 1992; Unadkat et al., 2009; Montante et al., 2012) and in Computational Fluid Dynamics (CFD) simulations (Joshi and Nandakumar, 2015; Werner et al., 2014; Wang et al., 2018). Nonetheless, the turbulent characteristics of the two phase-flow remain an open issue (Micheletti and Yianneskis, 2004).

Since the early 1990s, researchers have experimentally investigated the effect of particles on turbulence modulation (Crowe, 2000). According to the summary by Crowe et al. (1998), small particles attenuate turbulence and large particle enhance turbulence in the continuous phase. However, recent experimental investigations found contradicting results regarding the criterion applied by Crowe et al. (1998) in stirred tanks (Gabriele et al., 2011; Montante et al., 2012).

The lack of "CFD-grade" experimental data has hampered progress in the development of Euler-Euler CFD models of solid-liquid flows, and in particular the closure models for the turbulence effects. Due to the largely empirical nature of the closure models, their validity must be assessed by comparing the overall model predictions with experimental data. Several authors have described different closure relations and assessed them by comparing the results to different sets of experimental data, with a lack of comparability between the individual works (see the recent review in Shi and Rzehak (2020)). Despite the reasonable agreement over the limited range of conditions to which each model variant has been applied, no complete, reliable, and robust set of closure relations has emerged so far.

Ideally, a "CFD-grade" database for model validation should contain a comprehensive set of flow parameters, specifically the spatially resolved mean and fluctuation velocities of both phases as well as the solid fraction, which assess all aspects of the overall model. Moreover, some variation in the parameters such as particle size, particle to liquid density ratio, solid loading, and impeller rotation speed is necessary to accommodate a broad range of applications. Finally, the quantification of measurement errors is required. Statistical errors can be controlled by ensuring

*Corresponding author
Email address: a.sommer@hzdr.de (A.-E. Sommer)

that the measurement time is sufficiently long. Systematic errors are more difficult to assess but especially critical for model validation.

Available measurements satisfying the criteria above are limited. According to the recent review in Shi and Rzehak (2020), the works by Unadkat et al. (2009) and Nouri and Whitelaw (1992) are the only ones which simultaneously measured the flow field of both phases and the spatial distribution of the solid fraction. Unadkat et al. (2009) measured these parameters with Particle Image Velocimetry (PIV) and image analysis techniques. The experimental conditions were limited to glass spheres with a diameter of 1000 µm and one impeller rotation speed. Nouri and Whitelaw (1992) used a combination of Laser Doppler Anemometry (LDA) and reflection index matching techniques to achieve a wide range of experimental parameters with varying particle sizes, density ratios and volumetric concentrations. However, the particle size fraction differed between the particle materials, making the effect of the density ratio difficult to compare. Furthermore, fine particles with diameters smaller than 100 µm, which are widely used in froth flotation (e.g. Trahar and Warren, 1976), were not investigated. These limitations will be overcome by the current work.

In this present work, a "CFD-grade" database for the validation of numerical models is built for two types of particles with different values of solid-to-liquid density ratio ρ_S/ρ_L, namely polyethylene (PE, $\rho_S/\rho_L = 1.1$) and glass beads ($\rho_S/\rho_L = 2.5$). For each type of particle, three particle size groups (63 µm... 70 µm; 150 µm... 180 µm; 400 µm... 500 µm), four values of the mean solid volume fraction (0.025 vol%; 0.05 vol%; 0.075 vol%; 0.1 vol%), and three values of the impeller rotation speed (650 rpm; 1000 rpm; 1500 rpm) are considered. The velocity field of both phases was measured by a combination of PIV and Particle Shadow Velocimetry (PSV). The mean and fluctuating liquid and solid velocities were obtained by both time averaging and angle-resolved averaging (see Section 2 for the details). Additionally, the local solid fraction was calculated in the measurement plane.

The paper is organized as follows. The details of the presently used experimental setup and the applied measurement techniques are described in the next section. Section 3 outlines the single-phase flow simulations that are used to cross-check the experiments. Section 4 presents the main results and the comparison with the numerical simulations. A final summary and conclusions are given in Section 5. The description of the "CFD-grade" database is found in the appendix.

2. Experimental setup and measurement methods

2.1. Experimental setup: stirred tank

The experimental setup consist of a cylindrical stirred tank with a tank diameter, D_t, of 90 mm (Figure 1). The other dimensions of the setup are expressed as ratios to D_t as shown in Figure 1(a). The tank is placed in a square box filled with water to limit the optical distortion at the curved surface (Unadkat et al., 2009). Optical accessibility is ensured by using transparent polymethyl methacrylate (PMMA).

The particles are suspended by an overhead stirrer with a Rushton turbine (Eurostar 20 digital, IKA®-Werke GmbH & Co. KG, Germany). The diameter of the impeller, D_i, is 30 mm, and the impeller rotation speed, Ω, is set to 1500 rpm. Preliminary tests with higher impeller rotation speeds have shown an entrainment of air. Additional measurements at $\Omega = 650$ rpm and 1000 rpm are conducted to analyze the effect of the impeller rotation speed. Accordingly, the Reynolds number of the impeller, $Re_\Omega = \frac{\Omega D_i^2}{\nu}$, varies between 9717 and 22424, while the tip velocity, $u_{tip} = \pi \Omega D_i$, ranges between $1.02\,\mathrm{m\,s^{-1}}$ and $2.36\,\mathrm{m\,s^{-1}}$. The uncertainty of Ω is less than 1 % and the vibration of the impeller results in a radial shift by up to 0.5 mm.

Deionized water is selected as the liquid phase and polyethylene (PE) (Cospheric LLC, USA) and glass beads (SiLibeads solid Micro Glass Beads, Sigmund Lindner GmbH, Germany) are used for the solid phase (Table 1). In the case of PE, the particles are hydrophilized with Tween20 ($c = 1\,\mathrm{g\,l^{-1}}$, Sigma Aldrich, USA) before their suspension. Otherwise, the particles are too hydrophobic to be submerged in water. More specifically, the particles are mixed in the Tween20 solution until all particles are suspended in the solution. Afterwards, the particles are rinsed off with deionized water to remove excessive surfactant.

Besides the variation in the solid density, ρ_S, different particle size fractions are used – fine (63 µm... 70 µm), medium (150 µm... 180 µm) and coarse (400 µm... 500 µm) – resulting in a range of particle Reynolds numbers, Re_p, and Stokes numbers, St. The particle Reynolds number is defined as

$$Re_p = \frac{d_p u_{term,0}}{\nu}, \tag{1}$$

with the terminal velocity,

$$u_{term,0} = \sqrt{(4 d_p (\rho_S - \rho_L) g / (3 C_D \rho_L)}, \tag{2}$$

and the Schiller-Naumann drag coefficient $C_D = 24/Re_p(1+0.15Re_p^{0.687})$ (Schiller and Naumann, 1933). The Stokes number is the ratio of the particle relaxation time, τ_S, to the typical timescale of the stirred flow, τ_L,

$$St = \frac{\tau_S}{\tau_L} \tag{3}$$

with

$$\tau_L = \frac{H_{bla}}{u_{tip}} \tag{4}$$

(Nouri and Whitelaw, 1992), where H_{bla} denotes the blade height (Figure 1(a)), and

$$\tau_S = \frac{(\rho_S + 0.5\rho_L)}{\rho_L} \frac{4 d_p}{3 C_D u_{term,0}} \tag{5}$$

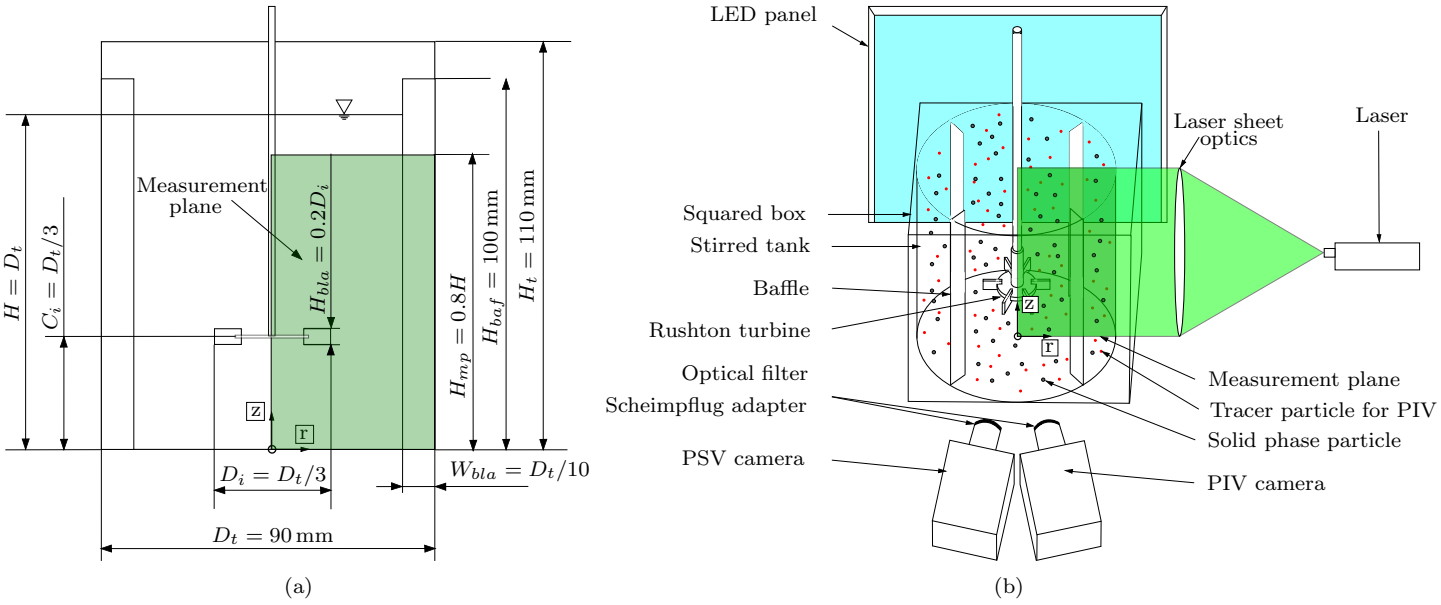

Figure 1: Experimental setup: (a) Dimensions of the stirred tank. (b) Arrangement of the stirred tank and the applied measurement technique.

for $Re_p < 1000$ (Sommerfeld, 2017).

The volume concentration of the solid phase, α_S, is limited by the optical access to the measurement plane. Therefore, only experiments with $\alpha_S \leq 0.1\,\%$ are conducted.

2.2. Measurement methods: PIV and PSV

For the simultaneous measurement of each phase, two cameras are used to capture each phase separately. Similarly to Unadkat et al. (2009) and Montante et al. (2012), light filters are used to block the light in the unwanted phase. In contrast to these authors, two different light sources (laser and light-emitting diode (LED) backlight) are used, leading to a combination of PIV and PSV as a measurement technique. The advantage of PSV for the measurement of the solid phase is that all particle materials can be used without any limitation. In contrast, PIV and LDA can only detect particles from their scattered light (e.g. glass particles), whereas PSV uses their shadow.

The basic idea of PIV is that sufficiently small and neutrally buoyant tracers follow the streamlines of the fluid flow with negligible deviation ($St \ll 0.1$, Samimy and Lele (1991)). Thus, the fluid velocity is assumed to be equal to the tracer velocity. The tracers in a defined measurement plane are illuminated by a laser sheet and the scattered light is captured in a time-resolved manner with a high-speed camera. The recorded images are cross-correlated to calculate the instantaneous velocity field, $\mathbf{u} = (u_r, u_z)^T$, in radial, r, and axial, z, directions. A detailed description of this method is given by Raffel et al. (2014).

In contrast, PSV measures the instantaneous velocity field of the solid phase and concentration based on the recorded shadow image of the particles, illuminated by a LED backlight. By using a small depth of field (DOF), particles in a thin area of the volume can be identified so that the particle displacement is evaluated in a quasi-2D measuring volume (Estevadeordal and Goss, 2005).

During the experiments, images are recorded with two CMOS cameras (Phantom VEO 410 L, spatial resolution 0.06 mm/pix) as seen in Figure 1(b). Both cameras use a Tokina Macro 100 F2.8D objective with a focal length of 100 mm. The PIV camera is equipped with an optical long pass filter ($\lambda_{pass} > 540\,\text{nm}$), to ensure the capturing of scattered light from the fluorescent PMMA tracers ($d_p = 20 - 50\,\mu\text{m}$; $\alpha_S \approx 0.07\,\text{vol}\%$). These tracers are colored with Rhodamin B ($\lambda_{abs} = 560\,\text{nm}/\ \lambda_{em} = 584\,\text{nm}$) and are excited by a Nd:YLF laser ($\lambda_{em} = 527\,\text{nm}$, Photonics Industry, USA). The thickness of the laser sheet is 1 mm.

In contrast, the PSV camera is equipped with an optical band pass filter ($400\,\text{nm} < \lambda_{pass} < 500\,\text{nm}$), to filter out the florescent tracers and capture only the solid phase. Therefore, the LED panel ($\lambda_{em} = 450\,\text{nm}$, LaVision, Germany) is placed behind the measurement plane. To minimize the DOF of the PSV images, the lowest f-number of $f/2.8$ is used. The DOF is calibrated with the method proposed by Goss and Estevadeordal (2006). All particle types are glued to a transparent plate. Their images are recorded at equidistant depth position using a translation stage. Figure 2 illustrates the relative peak intensity ratio between each particle and its surroundings. If the relative intensity drops below 0.1, the particle is out of focus, resulting in a DOF of twice the distance from the object plane.

Both cameras are aligned nearly perpendicular to the laser sheet to capture the same field of view. A Scheimpflug adapter is used to match the plane of focus of each camera with the measurement plane. The origin of the coordinate system is in the center of the base of the tank, with the

Symbol	Material	ρ_S in g cm^{-3}	d_p in µm	τ_S in s	St	Re_p
PE063	Polyethylene	1.1	63 – 70	$4.8 \cdot 10^{-7}$	$1.9 \cdot 10^{-4}$	0.02
PE150			150 – 180	$4.8 \cdot 10^{-5}$	$1.9 \cdot 10^{-2}$	0.4
PE425			425 – 500	$2.7 \cdot 10^{-3}$	1.1	4.5
GL063	Glass	2.5	63 – 70	$1.2 \cdot 10^{-5}$	$4.6 \cdot 10^{-3}$	0.3
GL150			150 – 180	$7.7 \cdot 10^{-4}$	0.3	4.3
GL400			400 – 450	$2.0 \cdot 10^{-2}$	7.9	34.6

Table 1: Properties of the particle systems used, consisting of density, ρ_S, size fraction, d_p, particle relaxation time, τ_S, Stokes number, St, and particle Reynolds number, Re_p.

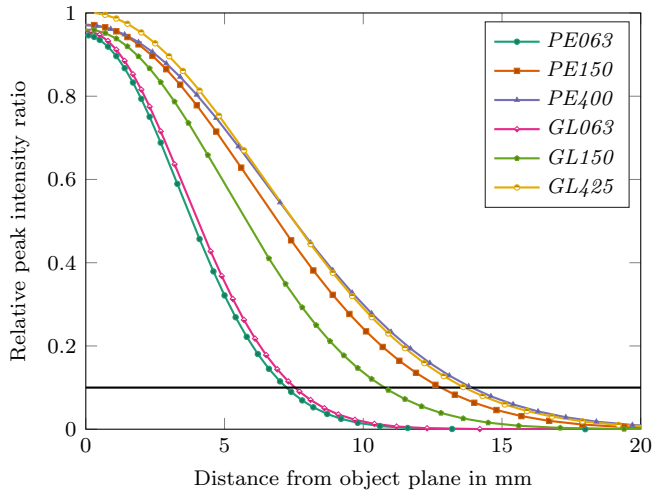

Figure 2: Diagram of the relative peak intensity over the distance from the object plane in the positive direction for all particle systems. The black line illustrates the threshold for depth of field (DOF), where the signal drops below 0.1 (Goss and Estevadeordal, 2006).

radial coordinate, r, pointing towards the tank wall, the axial coordinate, z, pointing perpendicular to the free surface of the liquid and the azimuthal angle denoted as θ. The measurement plane is located at $\theta = 0°$ midway between two baffles and includes only half of the tank diameter, taking advantage of the symmetry of the flow. However, there is a lack of data due to optical distortion of the baffles in the range of $0.48 \leq \frac{2r}{D_t} \leq 0.73$ for the PIV (see Figure 7) and $0.45 \leq \frac{2r}{D_t} \leq 1$ for the PSV images (see Figure 18(a)). The camera frame rate is chosen to ensure that the angle of the impeller rotation between two consecutive images is less than 2° and an integer multiple of the impeller rotation speed. Therefore, the camera frame rate is set to 4500 Hz(= 270 000 1/min) for $\Omega = 1000$ rpm and $\Omega = 1500$ rpm and 4550 Hz(= 273 000 1/min) for $\Omega = 650$ rpm.

2.3. Data analysis

The commercial Software DaVis 10.1 (LaVision, Germany) is used to calculate the instantaneous velocity field based on two time-resolved consecutive images. The recorded PIV and PSV images are processed in the same manner, except that the PSV images are inverted beforehand. First,

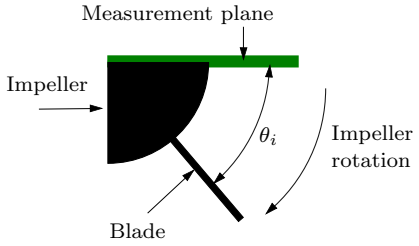

Figure 3: Definition of the angular position, θ_i, between the impeller blade and the measurement plane.

in preprocessing, the particle contrast is enhanced by subtracting the background, applying a Gauss filter (3x3) and sharpening the particles. The brightness is normalized over the measurement field in all images. Second, the impeller and baffles are masked out to minimize distortion due to reflections. Last, the enhanced images are evaluated using an interrogation window size of 32 pix × 32 pix after an iterative multigrid evaluation with interrogation window refinement.

The measured instantaneous velocity field is averaged to obtain its mean, $\overline{\mathbf{u}} = (\overline{u_r}, \overline{u_z})^T$, and fluctuation, $\mathbf{u}' = (u_r', u_z')^T$, components with $u_i' = \sqrt{R_{ii}}$, where R_{ii} denotes the Reynolds stress. The averaging is performed in two different manners, namely a time average, $\overline{\mathbf{u}(\mathbf{t})_\mathbf{T}}$, and an angle-resolved average, $\overline{\mathbf{u}(\mathbf{t})_\theta}$. The mean and fluctuation velocities obtained from the latter are represented by

$$\overline{u(t)_\theta} = \frac{1}{N(\theta = \theta_i)} \sum_{t=0}^{T} u(t, \theta = \theta_i),$$
$$R_{ij,\theta}(t) = \frac{1}{N(\theta = \theta_i)} \sum_{t=0}^{T} u_i'(t, \theta = \theta_i) \cdot u_j'(t, \theta = \theta_i), \quad (6)$$

with the definition of θ as illustrated in Figure 3 and N =500...800 images. The data analysis focuses on three angles: $\theta_0 = 0°$ in the plane coinciding with one of the impeller blades, $\theta_{24} = 24°$ in the wake region of the blade and $\theta_{48} = 48°$ approaching the next blade. The angular position of the blade is detected by image analysis. The maximum radial blade position for each pass is thus detected from the PSV images and defined as θ_0. θ_{24} and θ_{48} are then determined based on the frame rate and impeller rotation speed used. In this way, an uncertainty of the angular position of maximal 2° is reached.

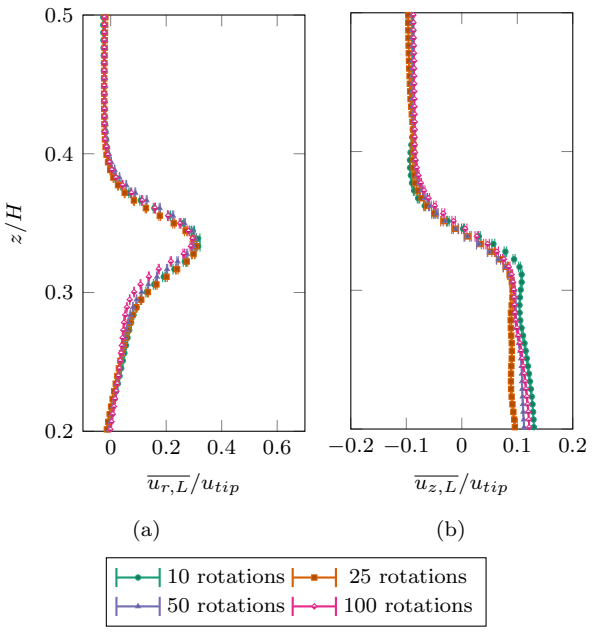

Figure 4: Sensitivity study of the number of rotations used for time averaging on the calculated radial (a) and axial (b) velocity profiles at $r = 0.44D_t/2$ and $\Omega = 1500\,\mathrm{rpm}$ in the single phase flow.

The time-average mean and fluctuations velocities are obtained by

$$\begin{aligned} \overline{u(t)_T} &= \frac{1}{T}\sum_{t=0}^{T} u(t), \\ R_{ij,T}(t) &= \frac{1}{T}\sum_{t=0}^{T} u_i'(t)\cdot u_j'(t), \end{aligned} \tag{7}$$

over 50 rotations as the result of the sensitivity study (Figure 4). This equals 9000…21 000 time steps, T, depending on the impeller rotation speed and the chosen frame rate.

During the measurements, random uncertainties occur, e.g., due to the particle image size, particle image density, turbulent fluctuations, and interrogation window size (Charonko and Vlachos, 2013; Kähler et al., 2012; Sciacchitano et al., 2015). Therefore, the uncertainties of the mean and fluctuation velocities are quantified as

$$E = s\sqrt{\frac{1}{N}} \tag{8}$$

with N denoting the number of samples and

$$s = \sqrt{\frac{1}{N-1}\sum_{i=1}^{N}(X_i - \overline{X})^2} \tag{9}$$

the standard deviation (Sciacchitano and Wieneke, 2016).

The calculation of the solid concentration is adapted from Unadkat et al. (2009) as the ratio of the accumulated particle volume, V_p, to the reference volume, V_{ref},

$$\alpha_S(r,z) = \frac{V_p}{V_{ref}} = \frac{n_p \cdot \overline{d_p}^3\,\pi/6}{V_{ref}} \cdot 100\%. \tag{10}$$

The accumulated particle volume is estimated from the number of particles, n_p, in the reference volume and their average diameter, $\overline{d_p}$, per time step. The number of particles in each reference volume, V_{ref}, of the PSV images is counted using the commercial software DaVis 10.1. Particle diameters much larger or smaller ($\pm 50\,\mu\mathrm{m}$) than the expected particle diameter are filtered out.

The reference volume is defined as a cuboid, $V_{ref} = (\Delta r \cdot \Delta z - A_{mask}) \cdot DOF$, with an edge length of 5 mm in both the radial and axial directions, i.e. with $\Delta r = \Delta z = 5\,\mathrm{mm}$. By proceeding in this manner, the measurement plane is split up into 9×18 elements. Whenever necessary, the masked-out area, $A_{mask} = n_{pix} \cdot \Delta^2$, is subtracted from the rectangular area, equaling the number of masked-out pixels, n_{pix}, times the squared spatial resolution, $\Delta = 0.06\,\mathrm{mm/pix}$.

3. Computational setup for single-phase flow simulations

Preliminary CFD simulations based on the Reynolds-averaged Navier–Stokes equations (RANS) approach are carried out for the single-phase flow conditions. In this case, the necessary modeling is restricted to turbulence and several previous experiences are available from the literature to judge the model quality. In the present work, the full Reynolds stress turbulence model developed by Speziale et al. (1991), hereafter referred to as the Speziale-Sarkar-Gatski (SSG) Reynolds stress model (RSM) model, is applied. As for the boundary conditions, no-slip is applied on the walls while free-slip is implemented at the top of the suspension. The simulations are performed using ANSYS CFX, release 19.2. The numerical setup corresponds with that of Shi and Rzehak (2018). The averages and fluctuations are calculated following the procedure discussed in Shi and Rzehak (2018) to match the experimentally obtained values. Other numerical details, i.e. the rotor-stator coupling, the SSG RSM model, and the grid independency study, are given in the following.

3.1. Moving reference frame (MRF) mixing-plane approach to rotor-stator coupling

The Reynolds-averaged Navier-Stokes equation for the single-phase flow reads

$$\begin{aligned} \frac{\partial}{\partial t}(\rho\overline{\mathbf{u}}) + \nabla\cdot(\rho\overline{\mathbf{u}}\otimes\overline{\mathbf{u}}) = -\nabla p + \nabla\cdot(2\mu^{mol}\mathbf{D}) \\ - \nabla\cdot(\rho\mathbf{R}) + \mathbf{F^{body}}. \end{aligned} \tag{11}$$

Here, $\overline{\mathbf{u}}$ is the mean velocity, p denotes the pressure, $\mathbf{D} = (\nabla\overline{\mathbf{u}} + (\nabla\overline{\mathbf{u}})^T)/2$ is the strain rate tensor, $\mathbf{R}$ is the Reynolds stress tensor, described below, and μ^{mol} is the molecular dynamic viscosity. Assuming an incompressible liquid, the density, ρ, is constant and the continuity equation simplifies to the incompressibility constraint, $\nabla\cdot\overline{\mathbf{u}} = 0$. The body force, $\mathbf{F^{body}}$, comprises gravity and in the case

ε equation	C_ε	$C_{\varepsilon 1}$	$C_{\varepsilon 2}$					
	0.18	1.45	1.83					
R equations	C_S	C_{1a}	C_{1b}	C_2	C_{3a}	C_{3b}	C_4	C_5
	0.22	3.40	1.80	4.20	0.80	1.30	1.25	0.40

Table 2: Coefficient values for the SSG RSM.

of a rotating reference frame also centrifugal and Coriolis forces. For the material properties, values at 25 °C are used, i.e. $\rho = 997\,\mathrm{kg\,m^{-3}}$ and $\mu^{mol} = 8.899 \times 10^{-4}\,\mathrm{kg\,m^{-1}\,s^{-1}}$.

To impose the no-slip condition not only on the rotating impeller and shaft but also on the fixed tank wall and baffles, the MRF method is employed. In this method, the tank is divided into two MRF blocks: a rotating one around the impeller and a static one comprising the rest of the fluid domain. Following the investigation by Shi and Rzehak (2018), the boundary between the two blocks is chosen to be the central point of the clearance between the impeller tips and baffles, and the rotating zone extends over the full tank height. The coupling between the two zones is achieved using the mixing-plane model, in which circumferentially averaged variables are passed between the blocks rather than strictly local ones (ANSYS, 2018).

3.2. SSG Reynolds stress model

The transport equation for the Reynolds stress tensor, $\mathbf{R} = \langle \mathbf{u}' \otimes \mathbf{u}' \rangle$, is given as

$$\frac{\partial}{\partial t}(\rho \mathbf{R}) + \nabla \cdot (\rho \overline{\mathbf{u}} \otimes \mathbf{R}) = \nabla \cdot ((\boldsymbol{\mu}^{\boldsymbol{mol}} + C_s \boldsymbol{\mu}^{\boldsymbol{turb}}) \nabla \otimes \mathbf{R}) + \rho(\mathbf{P} + \boldsymbol{\Phi} - \frac{2}{3}\varepsilon \mathbf{I} + \mathbf{G}), \quad (12)$$

and that for the turbulent dissipation rate ε as

$$\frac{\partial}{\partial t}(\rho \varepsilon) + \nabla \cdot (\rho \overline{\mathbf{u}} \varepsilon) = \nabla \cdot ((\boldsymbol{\mu}^{\boldsymbol{mol}} + C_\varepsilon \boldsymbol{\mu}^{\boldsymbol{turb}}) \cdot \nabla \varepsilon) + \rho \frac{\varepsilon}{k} \left(C_{\varepsilon,1} \frac{1}{2} tr(\mathbf{P}) - C_{\varepsilon,2} \varepsilon \right). \quad (13)$$

Individual terms appearing on the right side of Equation (12) describe diffusion, production, pressure-strain correlation, dissipation, and generation due to body forces (here, due to the rotating frame of reference used for the rotating MRF block).

Compared with isotropic two-equation turbulence models (for instance the $k-\omega$ Shear Stress Transport (SST) model), the diffusion term here involves tensorial viscosities such as

$$\boldsymbol{\mu}^{\boldsymbol{mol}} = \mu^{mol} \mathbf{I}, \quad (14)$$

$$\boldsymbol{\mu}^{\boldsymbol{turb}} = \frac{\rho k}{\varepsilon} \mathbf{R}, \quad (15)$$

the latter of which is anisotropic. The turbulent kinetic energy is related to the Reynolds stress as $k = 1/2\ tr(\mathbf{R})$. The turbulent dissipation rate, ε, is assumed to be isotropic. The production term, $\mathbf{P}$, is evaluated exactly in terms of the velocity gradient $\nabla \overline{\mathbf{u}}$ and $\mathbf{R}$, and its component notation reads

$$P_{ij} = -\left(\frac{\partial \overline{u_i}}{\partial x_k} R_{jk} + \frac{\partial \overline{u_j}}{\partial x_k} R_{ik} \right). \quad (16)$$

The generation term, $\mathbf{G}$, due to frame rotation is given in component notation as

$$G_{ij} = 2\mu^{mol} \Omega_k (D_{im} \varepsilon_{jkm} + D_{jm} \varepsilon_{ikm}), \quad (17)$$

where $\mathbf{D}$ is the strain rate tensor, $\boldsymbol{\Omega}$ the frame angular velocity, and ε_{ijk} is the Levi-Civita factor defined by

$$\varepsilon_{ijk} = \begin{cases} 1, & \text{if}(i,j,k)\text{are cyclic,} \\ -1, & \text{if}(i,j,k)\text{are anticyclic,} \\ 0, & \text{otherwise.} \end{cases} \quad (18)$$

Since $tr(\mathbf{G}) = 0$ from the definition in Equation (17), it does not appear in the equation for the turbulent dissipation rate, Equation (13).

Considerable caution has been taken in the modeling of the pressure-strain correlation $\boldsymbol{\Phi}$ due to its crucial role in redistributing the Reynolds stress components. According to Speziale et al. (1991), this term is given in component notation as

$$\begin{aligned} \Phi_{ij} = &- \left[C_{1a}\varepsilon + C_{1b} \frac{1}{2} tr(\mathbf{P}) \right] A_{ij} \\ &+ C_2 \varepsilon \left[A_{ik}A_{kj} - \frac{1}{3} A_{mn}A_{mn} \delta_{ij} \right] \\ &+ \left[C_{3a} - C_{3b}(A_{ij}A_{ij})^{\frac{1}{2}} \right] k D_{ij} \\ &+ C_4 k \left[A_{ik}D_{jk} + A_{jk}D_{ik} - \frac{2}{3} A_{mn}D_{mn}\delta_{ij} \right] \\ &+ C_5 k (A_{ik}W_{jk} + A_{jk}W_{ik}), \end{aligned} \quad (19)$$

where $\mathbf{A}$ and $\mathbf{W}$ denote the anisotropy and rotation rate tensors, respectively, with the components

$$A_{ij} = \frac{R_{ij}}{2k} - \frac{1}{3}\delta_{ij}, W_{ij} = \frac{1}{2} \left(\frac{\partial u_i}{\partial x_j} - \frac{\partial u_j}{\partial x_i} \right) + \varepsilon_{ijk} \cdot \Omega_k. \quad (20)$$

For the coefficients appearing in the equations above, the standard values of ANSYS CFX (ANSYS, 2018) are used as summarized in Table 2.

Mesh	Tank volume			Impeller blade			Overall	CPU time in h
	N_r	N_θ	N_z	N_r	N_θ	N_z	N_{tot}	
Mesh90	90	90	90	15	3	15	$7.29 \cdot 10^5$	25
Mesh144	144	144	144	24	5	24	$2.99 \cdot 10^6$	120
Mesh180	180	180	180	30	6	30	$5.83 \cdot 10^6$	200
Mesh240	240	240	240	40	8	40	$1.38 \cdot 10^7$	471

Table 3: Parameters for meshes used in grid independency study. The CPU time was calulated with 32 processors.

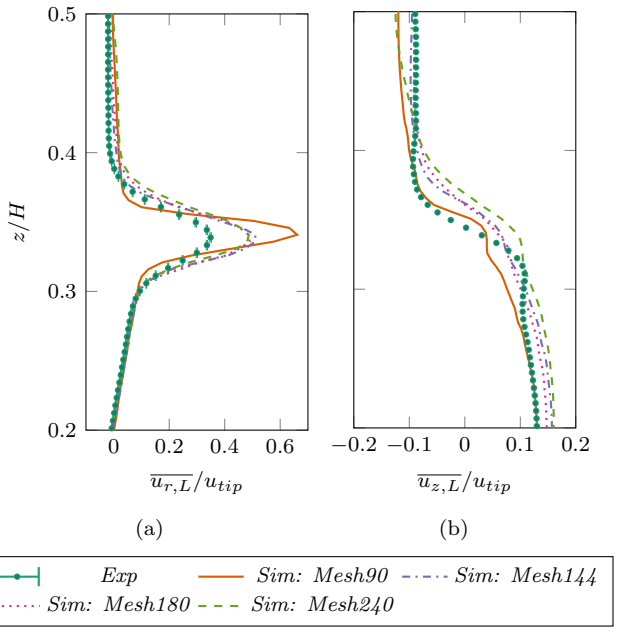

Figure 5: Results of grid independency study for the radial (a) and axial (b) components of the mean liquid velocity. The impeller rotation speed is 1500 rpm. Axial profiles restricted to a height range around the impeller are shown at the radial position of $2r/Dt = 0.44$.

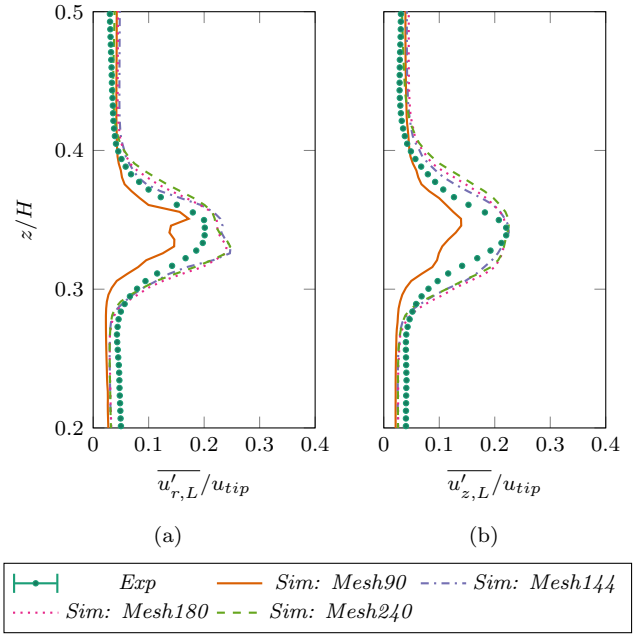

Figure 6: Same as Figure 5 but for the fluctuation velocity.

3.3. Grid independency study

For all tests, only half of the tank is considered as the solution domain, taking advantage of the periodicity of the flow. Four different grids with fully structured meshes are employed to ascertain the grid independence, as detailed in Table 3.

To illustrate the influence of the grid, the case with the highest impeller rotation speed, i.e., that is most critical, is considered. Results for the axial profiles of the radial and axial component of the time-averaged mean and fluctuation velocities at $2r/D_t = 0.44$ are considered in Figure 5 and Figure 6. These diagrams suggest that the grid independency has been achieved for *Mesh180*. The numerical settings described in Shi and Rzehak (2018, Section 4.2) are applied.

4. Results and description of database

4.1. Single-phase results

The single-phase flow results obtained experimentally will be discussed first to gain some insights into the flow field and compare with the CFD simulations. Both time-averaged and angle-resolved results comprising the mean and fluctuation velocities at various impeller rotation speeds will be introduced. For quantitative comparison of the experimental data with those obtained with simulation results, velocity profiles at two radial positions $2r/D_t = 0.44$ and $2r/D_t = 0.76$ are considered. The former is close to the impeller, and the latter is approximately midway between the impeller and the tank wall.

4.1.1. Mean flow field

Figure 7 gives an overview of the time-averaged liquid mean velocity (a) and the corresponding tangential vorticity (b) for the single-phase case at $\Omega = 1500$ rpm. The expansion of the impeller-induced jet and the entrainment of the surrounding fluid can be seen at the radial position $r = (0.3 \ldots 0.9)D_t/2$ and the axial position $z/H \approx \frac{1}{3}$. The peak mean velocity starts around the impeller blade, and decreases towards the tank wall. The minimum velocity of the jet is at the tank wall ($r > 0.9D_t/2$), leading to a redirection of the flow in upward and downward directions. Consequently, the characteristic vortices below and above the impeller are formed.

When the impeller rotation speed decreases, the result-

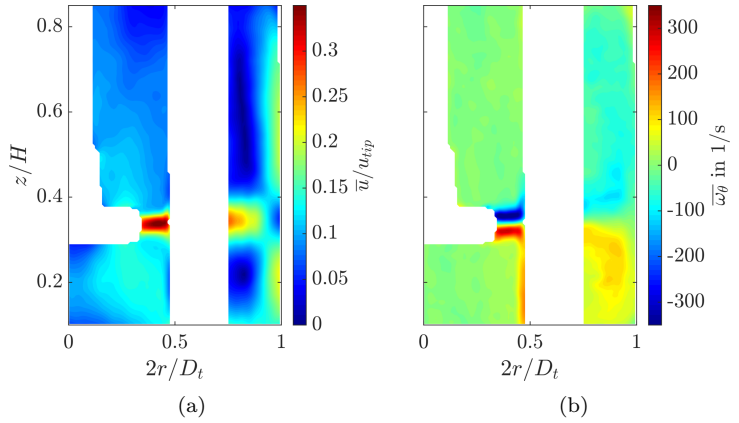

Figure 7: Time-averaged mean flow field of the single-phase case obtained experimentally at $\Omega = 1500\,\text{rpm}$. (a) Magnitude of the mean velocity, $\overline{u} = (\overline{u}_{T,r}^2 + \overline{u}_{T,z}^2)^{1/2}/u_{tip}$. (b) Tangential vorticity, $\overline{\omega_\theta} = \partial\overline{u}_{T,r}/\partial z - \partial\overline{u}_{T,z}/\partial r$, with negative $\overline{\omega_\theta}$ pointing outwards and positive $\overline{\omega_\theta}$ pointing inwards. The area of the impeller and baffles are masked out.

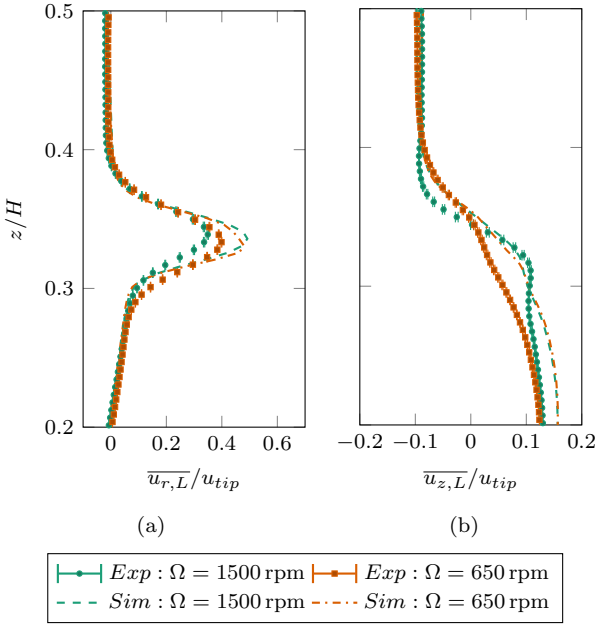

Figure 8: Effect of the impeller rotation speed on the time-averaged radial and axial mean velocity profile compared with single-phase simulation ($r = 0.44D_t/2$).]

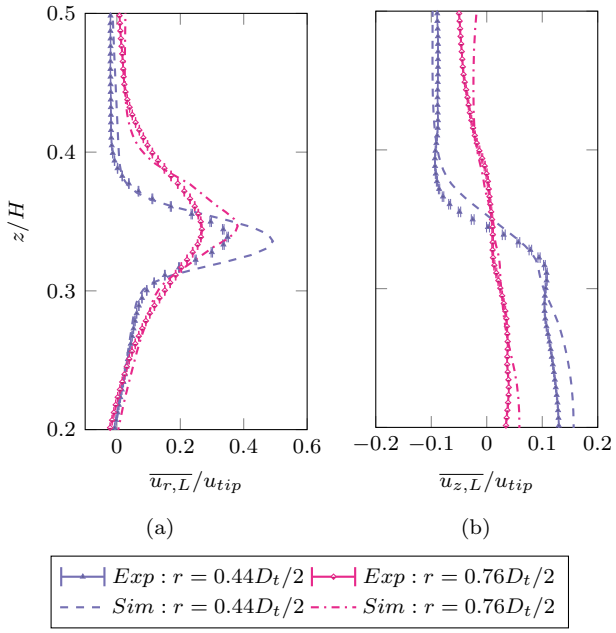

Figure 9: Influence of the radial position on the time-averaged radial and axial mean velocity profile compared with single-phase simulation ($\Omega = 1500\,\text{rpm}$).

ing variation in the mean flow field may be seen in Figure 8, where the time-averaged liquid mean velocities are plotted at the radial position $2r/Dt = 0.44$ for $\Omega = 650\,\text{rpm}$ and $\Omega = 1500\,\text{rpm}$. The peak of the radial velocity decreases slightly with increasing impeller rotation speed, whereas the axial velocity profile flattens in the jet core and becomes steeper at the edges. In the CFD simulations, the peak of the radial velocity and the axial velocity below the impeller are slightly overpredicted. The dependency of the velocities on the impeller rotation speed is not reproduced. However, the agreement between the simulation and experiment is still acceptable.

Another comparison is given in Figure 9, where results

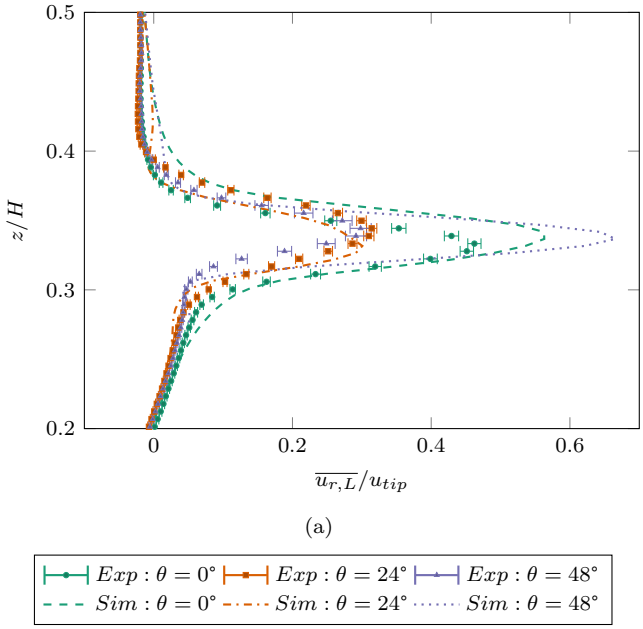

Figure 10: Effect of the angular position, θ_i, on the angle-resolved average of the radial mean velocity profile of the single phase flow compared with single-phase simulation ($\Omega = 1500\,\text{rpm}, r = 0.44D_i/2$).

at $\Omega = 1500\,\text{rpm}$ and $2r/Dt = 0.76$ are shown. As the distance from the impeller increases, the average velocities must decrease because of the expansion of the jet; this is confirmed by both the experimental and CFD results.

Results obtained from angle-resolved averaging allow the spatial structure of the flow field to be explored. Figure 10 illustrates the radial component of the angle-resolved liquid mean velocity at $\Omega = 1500\,\text{rpm}$ and $2r/Dt = 0.44$. The selected angles are $\theta = 0°, 24°, 48°$. As revealed from both the experimental and CFD simulation results, the peak values of the mean radial velocity at the intermediate position of $\theta = 24°$ are significantly lower than both $\theta = 0°$ and $\theta = 48°$. The change in the average velocity with the angular position may be understood by examining the distribution of the tangential vorticity (the so-called trailing vortex) at these selected slices. Figure 11(a) provides a qualitative illustration of the structure of the trailing vortex in the horizontal plane coinciding with the impeller disk, i.e. at $z/H = 0.33$. The tilting of the vorticity generated at the surface of the impeller blade by the velocity gradients associated in the upstream flow is known (Yianneskis et al., 1987) to cause a pair of trailing vortices in its wake (long curved arrows in Figure 11(a)). At $\theta = 0°$ (Figure 11(b)), the tail of the trailing vortices generated by the leading blade can be clearly observed. Further downstream, they have shifted away from the impeller, and thus can only be partially captured at $\theta = 24°$ (right side of Figure 11(c)). The pair of trailing vortices appearing on the left side of Figure 11(c) are certainly those generated by the trailing blade (Figure 11(a)) and remain sizable values further downstream, e.g. at $\theta = 48°$ (Figure 11(d)). Given that the two trailing vortices rotate in an anticlockwise direction, they cause an increase in the radial component of the local flow. As seen in Figure 11, at an angle $\theta = 24°$ (or $\theta = 48°$, respectively), the sampling position $2r/Dt = 0.44$ stands close to the center of the trailing vortex generated by the leading (trailing) blade. Thus, the peak of the corresponding liquid mean radial velocity at that position is larger than the time-averaged one.

Overall, the CFD simulation based on the models outlined in Section 3 agrees well with the experimental data. Shi and Rzehak (2020) also compared their numerical results with available experimental data and concluded that slight deviations occur until $Re_\Omega = 43320$. The maximum Reynolds number during these experiments was 22424, which is within this limit.

4.1.2. Turbulent fluctuations

Figures 12 and 13 illustrate the influence of the impeller rotation speed and the radial position on the time-averaged fluctuations, respectively. Similarly to the mean velocity, the dependency of the impeller rotation speed was analyzed at the radial position at $r = 0.44D_t/2$ with $\Omega = 1500\,\text{rpm}$. Overall, it is seen that the greatest fluctuations are around the impeller and the difference between the rotation speeds is small. The radial fluctuation profile at $\Omega = 650\,\text{rpm}$ shows a small double peak. This is likely connected with the presence of the pair of trailing vortices as seen in Figure 11. One reason why these are not resolved by the PIV measurements at $\Omega = 1500\,\text{rpm}$ is the higher velocity gradients and the larger angular movement between two consecutive images compared to the case at $\Omega = 650\,\text{rpm}$. Further away from the impeller, the fluctuations decrease (Figure 13) due to the dissipation by the fluid viscosity.

The spatially resolved field of flow fluctuation is illustrated in Figure 14 at position $r = 0.44D_t/2$ with an impeller rotation speed of $\Omega = 1500\,\text{rpm}$. In contrast to Figure 10, the highest radial fluctuations are at $\theta = 0°$ and the level decreases until $\theta = 48°$ in the experiments. The numerical results show a different picture, with the highest fluctuation at $\theta = 24°$ and the lowest at $\theta = 0°$. One reason for the variations between the experiments and numerical simulation in the angular position of the maximum radial fluctuation could be the uncertainty in the angular position and the oscillation of the impeller position in the axial direction due to the stirrer vibrations (Sharp and Adrian, 2001).

Overall, the results from the numerical simulations agreed well with the experimental results. Shi and Rzehak (2020) mentioned the high reliability of the simulated fluctuations until $Re_\Omega = 24300$, which includes precisely the experimental data proposed here.

4.2. Two-phase results

An overview of the available experimental data for two-phase flows is shown via contour plots of the mean velocity and their fluctuations. Here, the focus is on the time-averaged results at $\Omega = 1500\,\text{rpm}$. The angular averaged

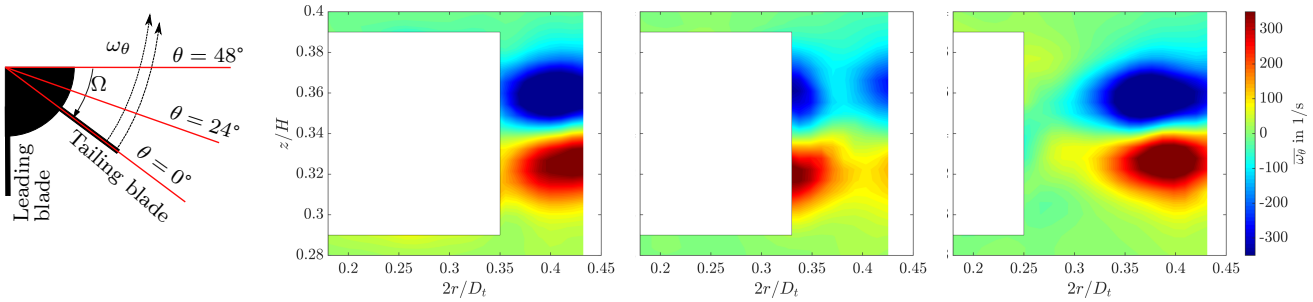

(a) (b) $\theta = 0°$ (c) $\theta = 24°$ (d) $\theta = 48°$

Figure 11: Moving trailing vortex formed by the impeller blade in the single phase flow at $\Omega = 1500\,\text{rpm}$. (a) Schematic of the structure of the trailing vortex. (b)-(d) Contour plots of the angle-resolved vorticity, $\overline{\omega_\theta}$ at the angular positions $\theta = 0°$, 24° and 48° as marked in the schematic structure (experimental data). The area of the impeller and baffles are masked out. The mask of the impeller blade changes due to the blade rotation.

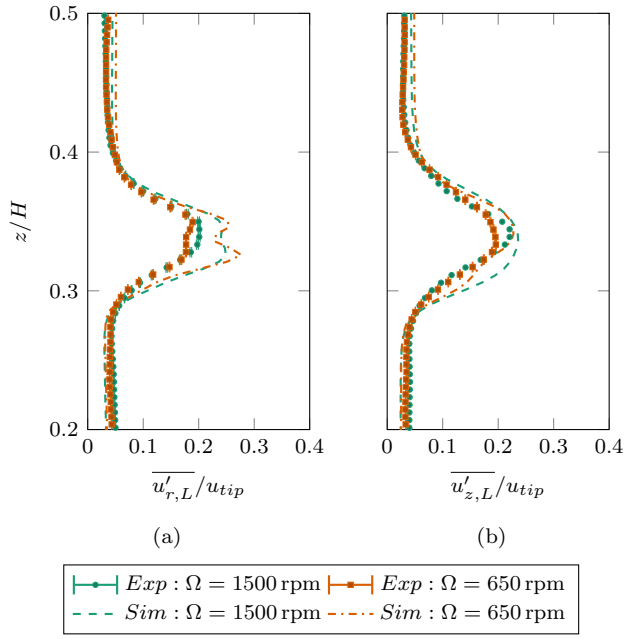

Figure 12: Effect of the impeller rotation speed on the time-averaged radial and axial fluctuation velocity profile compared with single-phase simulation ($r = 0.44D_t/2$).

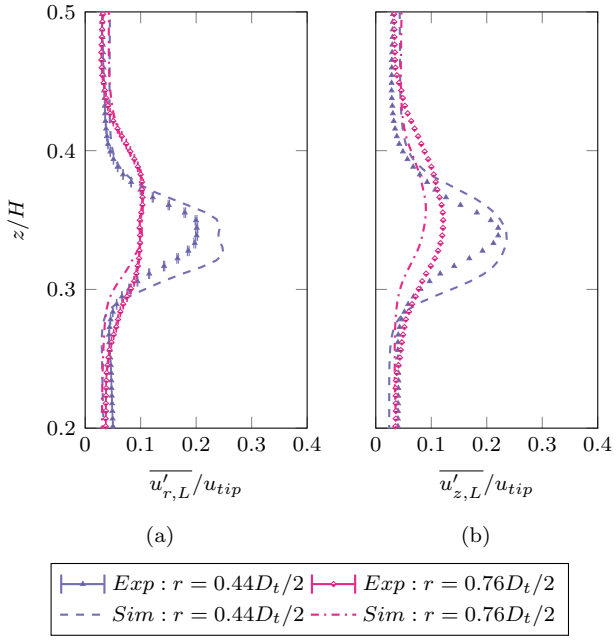

Figure 13: Effect of the radial position on the time-averaged radial and axial fluctuation velocity profile compared with single-phase simulation ($\Omega = 1500\,\text{rpm}$).

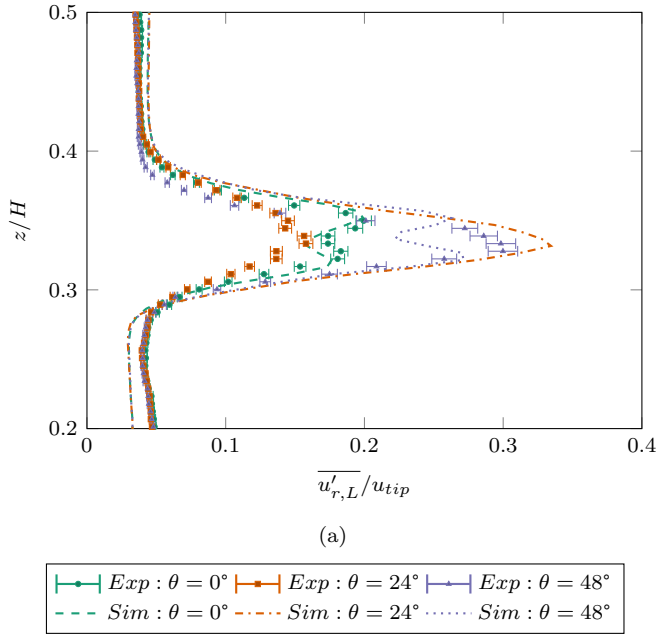

Figure 14: Effect of the angular position, θ_i, on the angular-resolved average of the radial fluctuation velocity profile of the single phase flow compared with single-phase simulation ($\Omega = 1500\,\text{rpm}, r = 0.44D_t/2$).

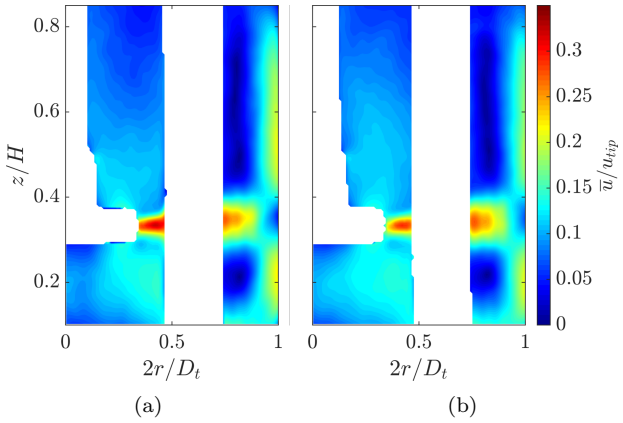

Figure 15: Magnitude of the time-averaged liquid velocity field of two-phase flow at $\Omega = 1500\,\text{rpm}$. (a) *PE063*, $\alpha_S = 0.025\,\text{vol\%}$ (b) *GL425*, $\alpha_S = 0.1\,\text{vol\%}$. The properties of the particle systems used are summarized in Table 1. The area of the impeller and baffles is masked out.

results are available in the database. The plots vary in terms of the particle size, material and solid fraction. Besides the liquid velocity fields, the solid velocity fields and local solid fractions are also discussed.

4.2.1. Liquid phase

Figure 15 illustrates the effect of particles on the liquid mean flow field. Here, the most distinct cases of the neutrally buoyant PE particles in the diameter range of fine particles were chosen, along with the lowest solid fraction ($\alpha_S = 0.025\,\text{vol\%}$) and the heavy glass beads in the diameter range of coarse particles and the highest solid fraction ($\alpha_S = 0.1\,\text{vol\%}$) Overall, the effect of the presence of the particles on the liquid mean velocity field is generally small because of the dilute system. Sommerfeld (2017) used the inter-particle spacing, $\frac{L}{d_p} = (\frac{\pi}{6\alpha_p})^{1/3}$, to classify the importance of interaction mechanisms and turbulence modulation (reduction or enhancement by the particles). During the experiments, the particle spacing, $\frac{L}{d_p}$, varied between 8 and 12.8, leading to a dilute system. Reference data for dense systems would also be suitable for a comprehensive database. However, the limitation in the transparency of the optical measurement technique prevented the measurement of particle systems with higher solid fractions. The PIV setups used by Montante et al. (2012) and Unadkat et al. (2009) allowed optical measurement up to $\alpha_S = 0.2\,\text{vol\%}$ and $\alpha_S = 0.5\,\text{vol\%}$, respectively. This was achieved by using large spherical glass particles of 774 µm and 1000 µm, respectively, resulting in a smaller number of particles in the measurement plane. The highest volume fraction of $\alpha_S = 1.5\,\text{vol\%}$ was achieved with the refractive index matching method proposed by Virdung and Rasmuson (2007). However, this method is only suitable for transparent materials such as glass beads.

Unlike the liquid mean velocity field, the fluctuation field of the liquid phase is strongly affected by the presence of the particles, as shown in Figures 16 and 17. The influence of the volume fraction is analysed for the fine particle system in Figure 16. For a low solid fraction, the fluctuation velocity of the liquid phase is reduced when the density of the particle is larger than that of the liquid (Figure 16(d)), while its magnitude is almost unchanged when the particle is nearly neutrally buoyant (Figure 16(b)). With an increasing solid fraction, the fluctuation velocity of the liquid phase is always enhanced (Figure 16(a) and (e)) compared to the single-phase case (Figure 16(c)). These findings agree with Montante et al. (2012), who found that the effect of turbulent modulation increases with a higher volume fraction. Further, lower radial fluctuation velocities of the liquid phase are observed below the impeller in Figure 16(e). This is mainly caused by the optical limitation of the measurement technique. As described in Section 4.2.2, the glass beads are not fully suspended. Therefore, below the impeller the solid concentration of these heavy particles is higher than that of the neutrally buoyant PE particles. The reduced transparency leads to higher uncertainties in the fluctuation velocities in this area for the heavier particles.

Depending on the material, the particle diameter has different effects on the radial fluctuation velocity field of the liquid phase. For the smaller particle diameters in the range of 63 µm to 70 µm, the radial fluctuations of the liquid phase in the jet region close to the impeller blade remain in the same order of magnitude compared to the single-phase flow. However, when the particle diameter increases to above 400 µm, the PE particles suppress the turbulence (Figure 17(a)), whereas the glass particles increase the turbulence (Figure 17(e)). Thus, we did not observe the

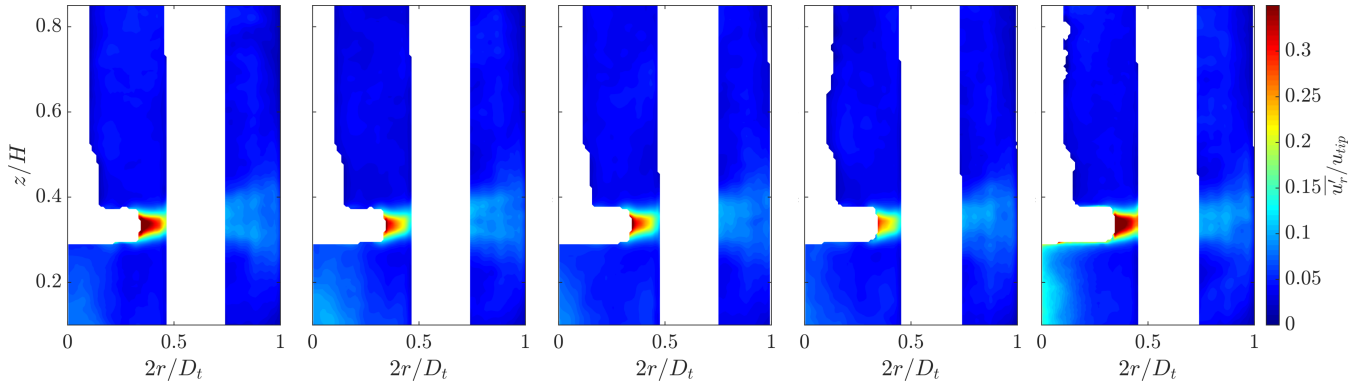

(a) 0.075 vol% (b) 0.025 vol% (c) Single Phase (d) 0.025 vol% (e) 0.075 vol%

Figure 16: Effect of the volume fraction of the solid phase on the radial component of the liquid fluctuation velocity. Particle system (a,b): *PE063*, (d,e): *GL063* ($\Omega = 1500\,\mathrm{rpm}$). The properties of the particle systems used are summarized in Table 1. The area of the impeller and baffles is masked out.

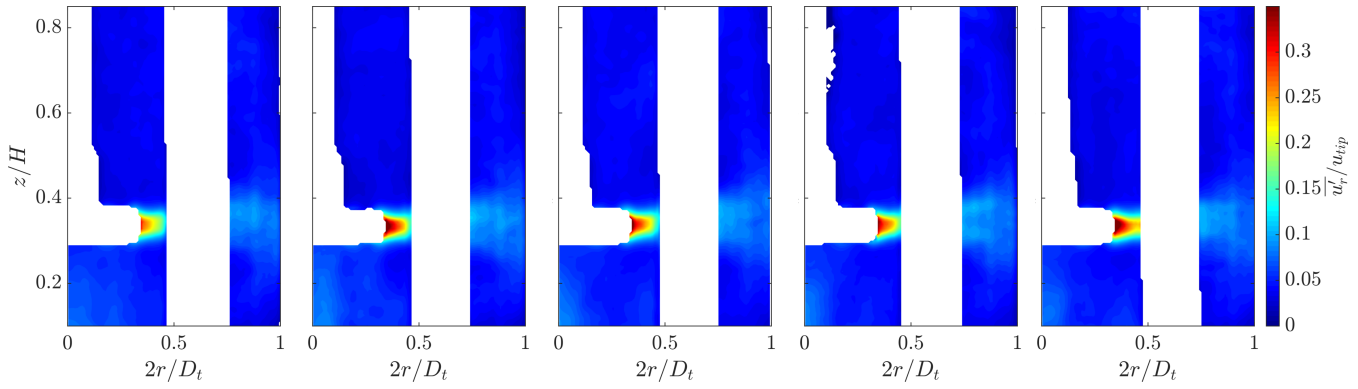

(a) (b) (c) (d) (e)

Figure 17: Effect of the particle diameter on the radial component of the liquid fluctuation velocity ($\alpha_S = 0.05\,\mathrm{vol\%}$, $\Omega = 1500\,\mathrm{rpm}$). (a) *PE400*. (b) *PE063*. (c) Single Phase. (d) *GL063*. (e) *GL425*. The properties of the particle systems used are summarized in Table 1. The area of the impeller and baffles is masked out.

turbulence of the liquid phase being directly modified by the particle diameter, in contrast to Gore and Crowe (1989). Gore and Crowe (1989) quantified the effect of particles on the turbulence by the ratio of the particle diameter to the integral length scale of the corresponding single-phase flow, d_p/Λ. According to their results, the turbulence intensity decreases for $d_p/\Lambda < 0.1$, and increases otherwise. In the present work, d_p/Λ ranged between 0.084 for the smaller particle diameters and 0.53 for the larger particle diameters close to the blade, with $\Lambda = 0.1D_i/4$ (Lee and Yianneskis, 1998), which should result in an enhancement of the turbulence by the larger particle fraction. It seems that not only the diameter but also the particle density plays a role. Montante et al. (2012) mentioned the uncertainty of this criterion. For instance, Unadkat et al. (2009) found a suppression of turbulence for $d_p/\Lambda = 0.285$.

4.2.2. Solid phase

The effect of the liquid flow on the solid particles is shown in Figure 18 and Figure 19. Here, the focus is on the axial mean and fluctuation velocity field for both phases, respectively. The particle systems of PE with $d_p = 63\,\mu\text{m} \ldots 70\,\mu\text{m}$ (Figure 18(a-b)) and glass with $d_p = 400\,\mu\text{m} \ldots 450\,\mu\text{m}$ (Figure 18(d-e)) are chosen as examples because of their high difference in terms of the Stokes number (Table 1).

For PE in Figure 18 (a,b), there is no significant difference between the solid and liquid velocity. The particles follow the flow completely ($St \ll 1$). In contrast, the axial velocity of the glass beads (Figure 18 (e)) is lower than the liquid mean flow velocity above and below the impeller (Figure 18 (d)). This case shows that the glass beads with the highest inertia are not fully suspended in the system, and the axial velocity is decreased due to the particle sedimentation. However, the correlation for complete suspension from Zwietering (1958) suggested an impeller rotation speed of 1500 rpm based on the geometry of the stirred tank and the two-phase flow properties for *GL425* ($\alpha_S = 0.1$ vol/percent). A further increase was impossible because of the formation of vortices if Ω exceeded 1600 rpm. Other researchers (Micheletti et al., 2003; Nouri and Whitelaw, 1992; Tamburini et al., 2013) encountered the same issue. However, in chemical reactors, there are many cases where a homogeneous or ultimate suspension is not desirable or difficult to realize with rapidly settling particles. These systems would lead to a high impeller speed and high energy dissipation. Therefore, models should also be able to predict partly suspended cases and evaluate whether these cases are more suitable in terms of energy consumption compared to the efficiency of transport (Kasat et al., 2008).

Comparison of the turbulent fluctuations between the liquid and solid phase (Figure 19) reveals that the axial turbulent fluctuation in the solid phase is lower than in the liquid phase. One reason lies in the experimental setup and the different DOF between PIV and PSV measurement techniques (Figure 2) - $DOF_{PSV} \approx 15\,\text{mm} \ldots 30\,\text{mm} >> DOF_{PIV} \approx 1\,\text{mm}$. Therefore, the fluctuations between the phases are not fully comparable with each other. Nonetheless, the data are still valuable for validating numerical simulations. For the numerical validation, the velocity fields have to be averaged over different depths, depending on the particle material and diameter. The same issue applies to the results for the solid concentrations.

For the liquid phase, the difference in the axial turbulent fluctuation between the two-phase flow (Figure 19 (b)+(d)) and single-phase flow (Figure 19 (c)) is small compared to the radial direction (Figure 17).

Figure 20 illustrates the local solid fraction for two particle systems (*PE400* and *GL425*) in the measurement plane close to the impeller ($2r/D_t < 0.5$) because of the large masked-out area close to the wall. In general, the neutrally buoyant PE particles are distributed quite evenly. The lower concentrations at $z/H \approx 1/3$ and near the bottom ($z/H \approx 0.1$) are caused by the impeller and reflections on the tank bottom, respectively. The heavy glass beads remain below the impeller confirming the partial suspension state of this particle system.

For both cases, the area of the masked-out impeller is smaller than in the velocity contour plots (e.g. Figure 19). This is caused by binning over an area of $5\,\text{mm} \times 5\,\text{mm}$ during the local solid fraction analysis, instead of $0.48\,\text{mm} \times 0.48\,\text{mm}$ during the PIV analysis.

In general, the systemic uncertainty is expected to be higher for the local solid fraction analysis than for the velocity analysis. On the one hand, overlapping particles lead to an underestimation of the local solid fraction. These particle agglomerations are wrongly detected as one large particle which is filtered out during the analysis. This systemic uncertainty increases with a higher number of particles in the measurement plane. Consequently, the coarse particle size range with the lowest volume fraction is less heavily affected than the fine particle fraction with the highest volume fraction.

On the other hand, the local solid fraction is sensitive to DOF because of its linear dependency on the reference volume. Although the DOF was quantified as seen in Figure 2 during the calibration with particles glued on a plate, the present DOF in the tank can differ from the calibrated one. During the measurements, the illumination of the particles was less steady than during the calibration. Therefore, shaded particles were filtered out during the image preprocessing, even though they were in the calibrated DOF. Thus, the reference volume during the measurements was smaller than calibrated, leading to an overestimation of the local solid fraction. Again, the coarse particle size range with the lowest volume fraction is less strongly affected than the fine particle fraction with the highest volume fraction.

To sum up, the fine particle systems have the highest systematic uncertainty in the analysis of the local solid fraction. In particular, their small particle diameter, below 70 µm, close to the spatial resolution limit of the image (60 µm), caused high uncertainties in the data analysis.

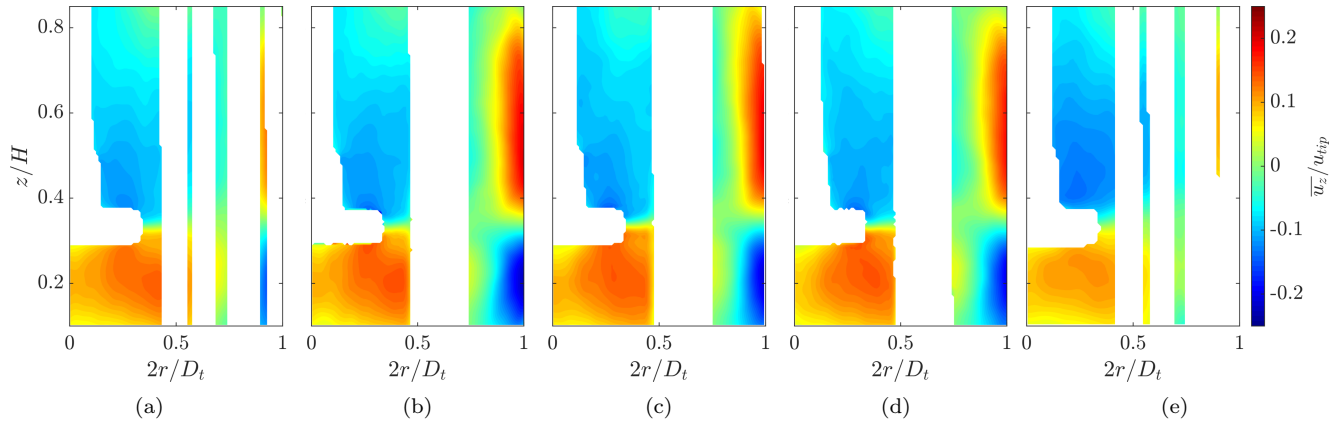

Figure 18: Effect of the Stokes number on the axial component of the liquid and solid mean velocity field ($\alpha_S = 0.05$ vol%, $\Omega = 1500$ rpm). (a) Solid phase of *PE063*. (b) Liquid phase of *PE063* (c) Single Phase. (d) Liquid phase of *GL425*. (e) Solid phase of *GL425*. The properties of the particle systems used are summarized in Table 1. The area of the impeller and baffles is masked out.

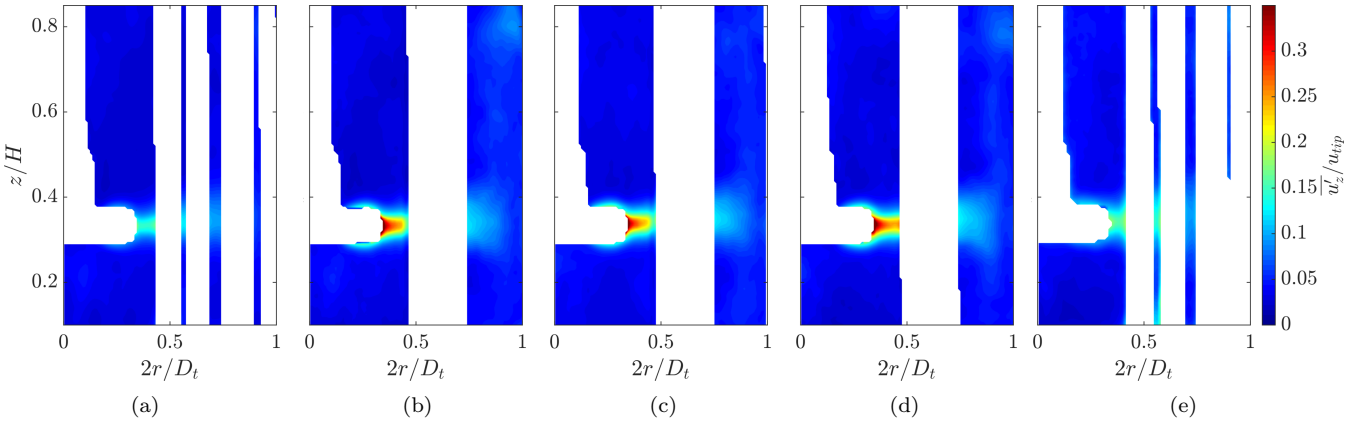

Figure 19: Effect of the Stokes number on the axial component of the liquid and solid fluctuation velocity ($\alpha_S = 0.05$ vol%, $\Omega = 1500$ rpm). (a) Solid phase of *PE063*. (b) Liquid phase of *PE063*. (c) Single phase. (d) Liquid phase of *GL425*. (e) Solid phase of *GL425*.The properties of the particle systems used are summarized in Table 1. The area of the impeller and baffles is masked out.

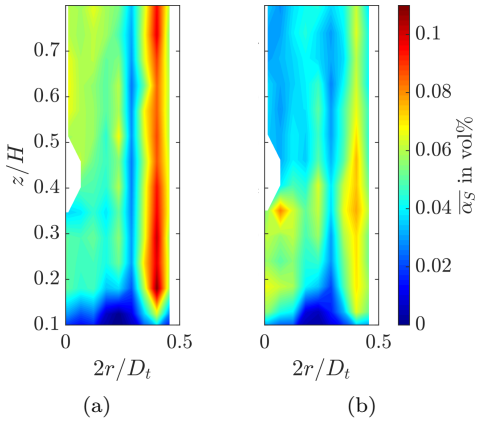

Figure 20: Local solid fraction for $\alpha_S = 0.05\,\text{vol}\%$ at $\Omega = 1500\,\text{rpm}$. (a) *PE400*. (b) *GL425*. The properties of the particle systems used are summarized in Table 1.

Therefore, the local solid fraction data analysis was focused on the particle systems of *PE150*, *PE400*, *GL150* and *GL425*, while *PE063* and *GL063* were neglected for this type of analysis.

In contrast to the systematic error, the statistical uncertainty of the local solid fraction analysis is in the same order of magnitude as for the velocity data: both used $500 - 800$ images for the angle-resolved averaging and $9000 - 21000$ time steps for the time-resolved averaging. This leads to a statistical uncertainty below 1 % for the local solid fraction analysis.

5. Summary and conclusions

This paper accumulates a database of "CFD-grade" data for the solid-liquid flow in a standardized stirred tank ($D_t = 90\,\text{mm}$), stirred by a Rushton turbine. This has been achieved by using a combined measurement technique of PIV and PSV to measure the liquid and solid velocity fields and the solid concentration simultaneously. This technique was applied for a wide range of experimental parameters including the density ratio, particle diameters, solid fractions and impeller rotation speeds (Table A.4). The data analysis applies not only a simple time average but also one that resolves the angular position for $\theta_i = 0°; 24°; 48°$ to show the spatial structures of the flow in the azimuthal direction. A summary of the experimental data and their quantified uncertainties is available under Rox et al. (2020) for use as validation data for closure models in CFD.

For the single-phase flow, numerical simulations were performed to cross-check the data. The SSG RSM turbulence model was adopted in conjunction with the mixing-plane MRF method. Comparisons of both the averaged mean and fluctuating velocities have shown that reasonably good predictions are obtained at $Re_\Omega < 2.3 \cdot 10^4$. This confirms the results gathered by Shi and Rzehak (2020), who reported a good reliability of the simulated averaged mean and fluctuation velocity until $Re_\Omega = 43320$ and $Re_\Omega = 24300$, respectively. Similar comparisons for the two phase flows will be given in a follow-up paper.

The experiments were conducted with a high number of samples to decrease statistical uncertainty, but some uncertainties still remain, for example the large DOF for the PSV in comparison to the PIV measurements and its variability regarding the particle diameter and material. In future studies, the sharpness of large particles could be detected by a threshold based on the gradient of the particle edges. For smaller particles, a camera objective with a larger focal length and a smaller aperture could decrease the overall DOF of the image (Goss and Estevadeordal, 2006).

The recorded data have a spatial and temporal resolution which is limited by the high impeller rotation speed. Therefore, high-velocity gradients, e.g. the double peak of the radial fluctuations (Figure 12(a)), are only partly resolved in the experiments.

Further, the application of optical measurement techniques is limited by the requirement of a transparent medium. Therefore, measurements with high solid fractions are challenging. To push the limit, a combination of a higher spatial resolution of the image and stronger backlighting would be possible to increase the visibility of the particles. In addition, techniques for matching the refractive index of the liquid and the dispersed phase could be used (Gabriele et al., 2011; Micheletti and Yianneskis, 2004; Nouri and Whitelaw, 1992).

To sum up, the generated database fulfills the criteria of "CFD-grade" data. Therefore, it closes a gap in previous experimental studies and allows the comprehensive assessment of closure models which is needed to finally arrive at a complete, reliable and robust formulation.

6. Acknowledgments

Mr. Pengyu Shi acknowledges support from the Chinese Scholarship Council (CSC). Computational resources were provided by HZDR. This project has received funding from the European Union's Horizon 2020 research and innovation program FineFuture under Grant Agreement No 821265.

Appendix A. Overview of database

All experimental data (Table A.4) described in this paper are stored as a database which is available under Rox et al. (2020). The data are structured into different folders and files as follows:

Level 1:Folders classified by flow system:

- *SinglePhase* or *ParticleMaterial-MinParticleDiameter* as outlined in Table 1

Level 2: Folders classified by measurement series: *Phase-RotationalSpeed-VolumeFraction-AverageMethod*

Material	d_p in µm	α_S in vol%	Ω in rpm
Single Phase	-	-	650; 1000; 1500
PE	63...70	0.025; 0.05; 0.075; 0.1	1500
	150...180	0.025; 0.05; 0.075; 0.1	650; 1000; 1500
	425...500	0.025; 0.05; 0.075; 0.1	1500
Glass	63...70	0.025; 0.05; 0.075; 0.1	1500
	150...180	0.025; 0.05; 0.075; 0.1	1500
	400...450	0.025; 0.05; 0.075; 0.1	1500

Table A.4: Overview of the cases investigated in the present work.

filename	averaged flow parameter $\overline{X}$	Unit
u_ r_ avg.csv	u_r/u_{tip}	-
u_ r_ fluc.csv	u'_r/u_{tip}	-
u_ z_ avg.csv	u_z/u_{tip}	-
u_ z_ fluc.csv	u'_z/u_{tip}	-
alpha_ s.csv	α_S	%

Table A.5: Overview of all averaged flow parameters, their filename and the unit in the database (Rox et al., 2020).

- *Phase:* L = liquid phase; S = solid phase
- *AverageMethods:*
  - *time* corresponds to time-resolved method (Equation (7))
  - *theta_X* corresponds to angle-resolved method (Equation (6)), where X represents the angle $\theta = 0°, 24°$ or $48°$

Level 3: csv files classified by their analysis parameter as defined in Table A.5

Each csv file consists of four columns, namely the normalized radial coordinate, $r_n = 2r/D_t$, the normalized axial coordinate, $z_n = z/H$, the averaged flow parameter, $\overline{X}$ (Table A.5), and the corresponding uncertainty, $\overline{X_{unc}}$. The uncertainty for each case was quantified as described in Equation (8).

References

ANSYS, I., 2018. ANSYS CFX User Guide: Release 19.2. Canonsburg, Pennsylvania.

Charonko, J.J., Vlachos, P.P., 2013. Estimation of uncertainty bounds for individual particle image velocimetry measurements from cross-correlation peak ratio. Measurement Science and Technology 24, 065301. doi:10.1088/0957-0233/24/6/065301.

Crowe, C., Sommerfeld, M., Tsuji, Y., 1998. Multiphase flows with drops and bubbles.

Crowe, C.T., 2000. On models for turbulence modulation in fluid-particle flows. International Journal of Multiphase Flow 26, 719–727. doi:10.1016/S0301-9322(99)00050-6.

Estevadeordal, J., Goss, L., 2005. PIV with LED: Particle Shadow Velocimetry (PSV). 43rd AIAA Aerospace Sciences Meeting and Exhibit doi:10.2514/6.2005-37.

Gabriele, A., Tsoligkas, A., Kings, I., Simmons, M., 2011. Use of PIV to measure turbulence modulation in a high throughput stirred vessel with the addition of high Stokes number particles for both up-and down-pumping configurations. Chemical engineering science 66, 5862–5874. doi:10.1016/j.ces.2011.08.007.

Gore, R., Crowe, C., 1989. Effect of particle size on modulating turbulent intensity. International Journal of Multiphase Flow 15, 279–285. doi:10.1016/0301-9322(89)90076-1.

Goss, L., Estevadeordal, J., 2006. Parametric characterization for Particle-Shadow Velocimetry (PSV). 25th AIAA Aerodynamic Measurement Technology and Ground Testing Conference doi:10.2514/6.2006-2808.

Joshi, J., Nandakumar, K., 2015. Computational modeling of multiphase reactors. Annual Review of Chemical and Biomolecular Engineering 6, 347–378. doi:10.1146/annurev-chembioeng-061114-123229.

Kasat, G., Khopkar, A., Ranade, V., Pandit, A., 2008. CFD simulation of liquid-phase mixing in solid-liquid stirred reactor. Chemical Engineering Science 63, 3877–3885.

Kähler, C.J., Scharnowski, S., Cierpka, C., 2012. On the uncertainty of digital PIV and PTV near walls. Experiments in Fluids 52, 1641–1656. doi:10.1007/s00348-012-1307-3.

Lee, K.C., Yianneskis, M., 1998. Turbulence properties of the impeller stream of a rushton turbine. AIChE J. 44, 13. doi:10.1002/aic.690440104.

Micheletti, M., Nikiforaki, L., Lee, K.C., Yianneskis, M., 2003. Particle concentration and mixing characteristics of moderate-to-dense solid-liquid suspensions. Industrial & Engineering Chemistry Research 42, 6236–6249. doi:10.1021/ie0303799.

Micheletti, M., Yianneskis, M., 2004. Study of fluid velocity characteristics in stirred solid-liquid suspensions with a refractive index matching technique. Proceedings of the IMechE 218, 191–204. doi:10.1243/0954408042466945.

Montante, G., Paglianti, A., Magelli, F., 2012. Analysis of dilute solid-liquid suspensions in turbulent stirred tanks. Chemical Engineering Research and Design 90, 1448–1456. doi:10.1016/j.cherd.2012.01.009.

Nouri, J., Whitelaw, J., 1992. Particle velocity characteristics of dilute to moderately dense suspension flows in stirred reactors. International journal of multiphase flow 18, 21–33. doi:10.1016/0301-9322(92)90003-Y.

Raffel, M., Wereley, S.T., Willert, C.E., Kompenhans, J., 2014. Particle Image Velocimetry. Springer Berlin Heidelberg.

Rox, H., Sommer, A.E., Eckert, K., Shi, P., Rzehak, R., 2020. "cfd-grade" experimental data for solid-liquid flow in a stirred tank. doi:10.14278/rodare.263.

Samimy, M., Lele, S.K., 1991. Motion of particles with inertia in a compressible free shear layer. Physics of Fluids A: Fluid Dynamics 3, 1915–1923. doi:10.1063/1.857921.

Sardeshpande, M., Ranade, V., 2012. Computational fluid dynamics modelling of solid suspension in stirred tanks. Current Science 102, 1539–1551.

Schiller, L., Naumann, A., 1933. About the basic calculations in gravity processing. Z. Ver. dtsch. Ing. , 318–321.

Sciacchitano, A., Neal, D.R., Smith, B.L., Warner, S.O., Vlachos, P.P., Wieneke, B., Scarano, F., 2015. Collaborative framework for PIV uncertainty quantification: comparative assessment of methods. Measurement Science and Technology 26, 074004. doi:10.1088/0957-0233/26/7/074004.

Sciacchitano, A., Wieneke, B., 2016. PIV uncertainty propagation. Measurement Science and Technology 27. doi:10.1088/0957-0233/27/8/084006.

Sharp, K., Adrian, R., 2001. PIV study of small-scale flow structure around a rushton turbine. AIChE Journal 47, 766–778. doi:10.1002/aic.690470403.

Shi, P., Rzehak, R., 2018. Bubbly flow in stirred tanks: Euler-euler/rans modeling. Chemical Engineering Science 190, 419–435. doi:10.1016/j.ces.2018.06.001.

Shi, P., Rzehak, R., 2020. Solid-liquid flow in stirred tanks: Euler-euler/RANS modeling. Chemical Engineering Science 227, 115875. doi:10.1016/j.ces.2020.115875.

Nomenclature

Greek formula characters

α	phase fraction
Δ	spatial resolution
$\Delta r/\ \Delta z$	edge length of reference volume in radial or axial direction
δ_{ij}	Kronecker delta
ε	turbulent dissipation rate
ε_{ijk}	Levi-Chivita factor
Λ	integral length scale
λ_{abs}	absorption wavelength
λ_{em}	emission wavelength
λ_{pass}	passing wavelength
μ	dynamic viscosity
ν	kinematic viscosity
ω	flow vorticity
Ω	impeller rotation speed
$\Phi_{ij}, \mathbf{\Phi}$	pressure-strain correlation
ρ	density
τ_L	time scale of the stirred of the stirred tank
τ_S	particle relaxation time
θ	azimuthal angle

Indices

$body$	on body
i, j	cartesian vector / tensor components
$inter$	on interface
L	liquid phase
mol	molecular
S	solid phase
$turb$	turbulent

Latin formula characters

$A_{ij}, \mathbf{A}$	anisotropy tensor
A_{mask}	masked out area
c	mass concentration
C_D	drag coefficient
C_i	clearance between the turbine and tank bottom
D_i	impeller diameter
$D_{ij}, \mathbf{D}$	strain rate tensor
d_p	particle diameter
D_t	tank diameter
E	Uncertainty
$F_{ij}, \mathbf{F}$	force per unit volume
g	acceleration of gravity
G_{ij}, G	generation term
H	tank filled height
H_{baf}	baffle height
H_{bla}	blade height
H_{mp}	height of measurement plane
H_t	tank height
$\mathbf{I}$	identity tensor
k	turbulent kinetic energy
N	number of grid cells/ images/ samples
n_p	number of particles
n_{pix}	number of pixels
p	pressure (static)
P	production term
r	radial coordinate
$R_{ij}, \mathbf{R}$	Reynolds stress tensor
Re	Reynolds number
Re_p	particle Reynolds number
Re_Ω	Reynolds number based on particle rotation rate
s	standard deviation
St	Stokes number
t	time
T	Time step
$u, \mathbf{u}$	resolved velocity
$\overline{u}, \overline{\mathbf{u}}$	averaged velocity
$u', \mathbf{u}'$	fluctuating velocity
u_{rel}	slip velocity
$u_{term,0}$	stagnant terminal velocity
u_{tip}	impeller tip velocity
V_p	particle volume
V_{ref}	reference volume
W_{baf}	baffle width
W_{bla}	blade width
$W_{ij}, \mathbf{W}$	rotation rate tensor
z	axial coordinate

Sommerfeld, M., 2017. Numerical methods for dispersed multiphase flows, in: et al., T.B. (Ed.), Particles in Flows, Springer. p. 327. doi:10.1007/978-3-319-60282-0_6.

Speziale, C.G., Sarkar, S., Gatski, T.B., 1991. Modelling the pressure-strain correlation of turbulence: an invariant dynamical systems approach. Journal of Fluid Mechanics 227, 245–272. doi:10.1017/S0022112091000101.

Tamburini, A., Cipollina, A., Micale, G., Brucato, A., 2013. Particle distribution in dilute solid liquid unbaffled tanks via a novel laser sheet and image analysis based technique. Chemical Engineering Science 87, 341–358. doi:10.1016/j.ces.2012.11.005.

Trad, Z., Vial, C., Fontaine, J.P., Larroche, C., 2015. Modeling of hydrodynamics and mixing in a submerged membrane bioreactor. Chemical Engineering Journal 282, 77–90. doi:10.1016/j.cej.2015.04.119.

Trahar, W., Warren, L., 1976. The flotability of very fine particles - a review. International Journal of Mineral Processing 3, 103–131. doi:10.1016/0301-7516(76)90029-6.

Unadkat, H., Rielly, C., Hargrave, G., Nagy, Z., 2009. Application of fluorescent PIV and digital image analysis to measure turbulence properties of solid-liquid stirred suspensions. Chemical Engineering Research and Design 87, 573–586. doi:10.1016/j.cherd.2008.11.011.

Virdung, T., Rasmuson, A., 2007. Solid-liquid flow at dilute concentrations in an axially stirred vessel investigated using particle image velocimetry. Chemical Engineering Communications 195, 18–34. doi:10.1080/00986440701554988.

Wang, G., Ge, L., Mitra, S., Evans, G.M., Joshi, J.B., Chena, S., 2018. A review of cfd modelling studies on the flotation process. Minerals Engineering 127, 153–177. doi:10.1016/j.mineng.2018.08.019.

Werner, S., Kaiser, S., Kraume, M., Eibl, D., 2014. Computational fluid dynamics as a modern tool for engineering characterization of bioreactors. Pharmaceutical Bioprocessing 2, 85–99. doi:10.4155/PBP.13.60.

Wu, J., Wang, S., Graham, L., Parthasarathy, R., Nguyen, B., 2011. High solids concentration agitation for minerals process intensifi-

cation. AIChE Journal 57, 2316–2324. doi:10.1002/aic.12468.

Yianneskis, M., Popiolek, Z., Whitelaw, J., 1987. An experimental study of the steady and unsteady flow characteristics of stirred reactors. Journal of Fluid Mechanics 175, 537–555. doi:10.1017/S002211208700051X.

Zwietering, T., 1958. Suspending of solid particles in liquid by agitators. Chemical Engineering Science 8. doi:10.1016/0009-2509(58)85031-9.